









High-Precision Control Method for High-Power MRI Gradient Power Amplifiers

Keqiu Zeng , Member, IEEE, Saijun Mao , Senior Member, IEEE, Gert Rietveld , Senior Member, IEEE, Jelena Popovic , Member, IEEE, Hui Yu , Member, IEEE, Ligu Wang , Member, IEEE, Kun Liu , Member, IEEE, and Zhiding Zhou , Member, IEEE

Abstract—In magnetic resonance imaging (MRI), high-power gradient power amplifiers (GPAs) are required to drive the gradient coils to generate strong and high-fidelity gradient fields. High precision is an essential requirement for the GPAs since precision directly impacts MRI imaging quality. Various aspects of the GPA have been the subject of research in the past years; however, high-precision GPA control that meets the stringent requirements of MRI applications is still a challenge. This article proposes a novel multi-rational-delay variables state space control method and an efficient out-of-band signal injection method to achieve GPA control accuracy at the level of one part per million at MVA output power levels. First, a systematic modeling and design method of the state space controller for high-power GPA is introduced utilizing state vectors with multi-rational-delay variables. This method improves the GPA dynamic performance significantly. Second, an efficient out-of-band signal injection method is presented to further improve the control precision at low output current, enabling the fulfillment of the challenging high-precision MRI requirements over the full GPA output range. Finally, the high-precision control method is validated in a GPA demonstrator with 500 A/1000 V output. Key results are a 30% improvement in current pulse reproducibility with respect to the conventional control method and a factor of 2.5 less noise at low currents. These experimental results validate the proposed novel method for the high-precision control of GPAs in

MRI applications and prove its capability to contribute to significantly improved MRI image quality.

Index Terms—Gradient power amplifier (GPA), high-precision control, magnetic resonance imaging (MRI), state space.

I. INTRODUCTION

GRADIENT power amplifiers (GPAs) are key components of magnetic resonance imaging (MRI) systems, as their performance directly impacts the MRI image quality. A diagram of the basic components and the architecture of an MRI system is illustrated in Fig. 1 [1], which contains three high-power GPAs to acquire the MRI signals in x , y , and z orientation to construct the raw data space of an MRI image. The interval between raw data points (ΔK) is determined by the area of a GPA trapezoid current pulse, as illustrated in Fig. 2 [2]. In order to achieve the accurate MRI image, GPAs must generate high-precision trapezoid current pluses at MVA power level with minimum amplitude variation and overshoot. For accurate imaging, the pulse areas need to be as close as possible in value within one MRI scan. This can be defined as the current pulse reproducibility to achieve the desired intervals (ΔK). To reach 7 μ As current pulse reproducibility in an MRI scan with 500 A current and 40 ms current integration time for each pulse, a precision requirement of 175 μ A is required, which is at the level of one part per million (ppm). Moreover, the GPA latencies also need to be very similar (within 200 ns) for the pulses in an MRI scan, in order to realize accurate excitations [2].

Generally, a high-precision GPA is composed of a power stage and a control stage. Early generations of GPA power stage consist of a full-bridge switching inverter in series with a linear mode amplifier [3]–[6]. However, the linear-mode amplifier suffers from large losses, making it difficult to apply in high-power applications. To solve this problem, a cascaded multilevel H-bridge topology is proposed in [3]–[15], which is the most-often-used topology in GPA because of its advantages of higher switching frequency, lower ripple current, and flexibility in power level. The precision achieved by a GPA greatly depends on the way that the control method is implemented. Multiple control approaches have been proposed in [4]–[8] and [12]–[18]. A control method with the classical proportional–integral–differential (PID) feedback and feedforward is proposed in [4]–[8]. A classical PID control method is also proposed for a similar application of nanoscale-precision positioning [12], [13]. Multiple solutions have been proposed to overcome the challenges caused

Manuscript received November 2, 2021; revised January 13, 2022; accepted February 19, 2022. Date of publication March 3, 2022; date of current version April 28, 2022. This work was supported in part by Philips Healthcare (Suzhou) Company, Ltd., in part by the University of Twente, in part by Fudan University, and in part by Shanghai Pujiang Program under Grant 20PJ1401500. Recommended for publication by Associate Editor M. Hartmann. (Corresponding author: Saijun Mao.)

Keqiu Zeng is with Philips Healthcare (Suzhou) Company, Ltd., Suzhou 215021, China, and also with the Faculty of Electrical Engineering, Mathematics and Computer Science, University of Twente, 7522 NB Enschede, The Netherlands (e-mail: keqiu_zeng@163.com).

Saijun Mao is with the Academy for Engineering and Technology, Center for Shanghai Silicon Carbide Power Devices Engineering and Technology Research, Fudan University, Shanghai 200433, China (e-mail: maosaijun@126.com).

Gert Rietveld is with the Faculty of Electrical Engineering, Mathematics and Computer Science, University of Twente, 7522 NB Enschede, The Netherlands, and also with VSL, 654 2600 Delft, The Netherlands (e-mail: g.rietveld@utwente.nl).

Jelena Popovic is with the Faculty of Electrical Engineering, Mathematics and Computer Science, University of Twente, 7522 NB Enschede, The Netherlands (e-mail: j.popovic@utwente.nl).

Hui Yu, Ligu Wang, Kun Liu, and Zhiding Zhou are with Philips Healthcare (Suzhou) Company, Ltd., Suzhou 215021, China (e-mail: yuhui5095@163.com; wlg123572_2@163.com; liu_kun76@163.com; zzd1992ah@163.com).

Color versions of one or more figures in this article are available at <https://doi.org/10.1109/TPEL.2022.3155686>.

Digital Object Identifier 10.1109/TPEL.2022.3155686

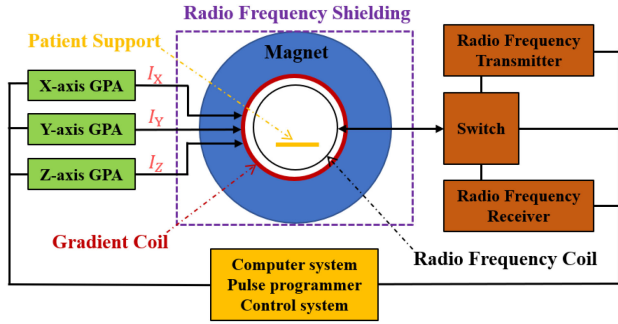


Fig. 1. Basic components and architecture of an MRI system [1].

by different kinds of disturbances and power loss. Common mode noise and internal common mode resonance for GPAs are analyzed in [19]. Also, various pulsewidth modulation (PWM) technologies and multiple topologies [6]–[8], [16]–[24] have been developed to bring different advantages: phase shifting PWM and auxiliary-resonant-commutated-pole enable the soft switching, reducing the disturbance generated by switching transitions and improving system efficiency; the space vector modulation method reduces common mode voltage, achieving low noise design; the carrier-wave shifted sinusoidal PWM inverter allows each H-bridge to operate in the same mode, distributing the power loss evenly among H-bridges. Furthermore, deadtime compensation is a commonly used approach to reduce the impact of interferences in the dynamic operation of the GPA [25]–[29].

However, a systematic method for designing the high-precision digital control of GPA and effective control methods to ensure the fulfillment of the high-precision requirements over the full output range of the GPA have not been studied in the literature. Moreover, none of the methods published so far are suited for improving the precision at low GPA output currents due to the asymmetrical switching disturbance and the nonlinearity effect. Therefore, further research into more suitable methods for the high-precision GPA control is necessary, which is the focus of this article.

In this article, a systematic design method for the precise digital control of high-power GPAs is developed to meet the stringent requirements of MRI. Particularly, a design approach for a multi-rational-delay variables state space controller is proposed, enabling the improvement of dynamic performance and the reduction of overshoot. Moreover, a critical influence factor affecting the precision at low GPA output currents is analyzed in detail. An effective solution for reducing the disturbance and nonlinearity effect that so far is unresolved by existing methods in the literature.

The rest of this article is organized as follows. Section II introduces the comprehensive design method of the multi-rational-delay variables state space control system. Section III proposes the analysis and solution to improve the GPA current precision at low output currents. Section IV validates the proposed methods with experimental results achieved in a GPA demonstrator based on the proposed approach. Finally, Section V concludes this article.

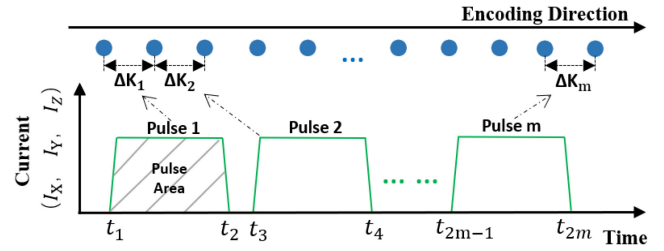


Fig. 2. One line of the raw data acquisition (blue dots) in an MRI scan with the typical GPA trapezoid output current pulses (green) [2]. $\Delta K_m = r \int_{t_{2m-1}}^{t_{2m}} I(t) dt$, where r is a constant.

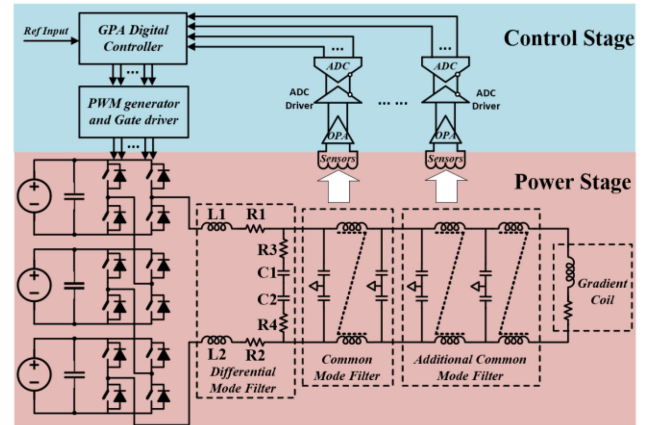


Fig. 3. Simplified circuit diagram of the MRI GPA with gradient coil, including the power stage (brown, bottom) and the control stage (blue, top).

II. DESIGN OF MULTI-RATIONAL-DELAY VARIABLES STATE SPACE CONTROL SYSTEM

A. Modeling Method for GPA

A cascaded H-bridge topology, the most-often-used topology for GPAs [3]–[15], is chosen as a demonstrator to describe the design method of the multi-rational-delay variables state space controller for GPAs. The diagram of the GPA system is shown in Fig. 3. It consists of three cascaded H-bridges, which are fed by three independent power supplies. The output of the cascaded H-bridge is filtered by an output filter, consisting of three stages: a differential mode filter and two common mode filters. The gradient coil can be represented by an equivalent inductance and resistor. For the development of the proposed control method, the common mode filters can be eliminated due to their limited impact on the modeling. Moreover, the low-pass differential filter has a floating ground potential, leading to a split point between the capacitors C_1 and C_2 . Therefore, the filter elements L_1 , L_2 , C_1 , C_2 , R_3 , and R_4 can be merged into one inductor, one capacitance, and one resistor. Besides this, R_1 and R_2 are small compared to the damping resistors R_3 and R_4 , and therefore can be omitted. The resulting simplified model of a GPA power stage is shown in Fig. 4. A zero-order hold approximation is used in this model in which the H-bridge output voltage can be represented by the multiplication of the total dc voltage (U_{DC}) and the duty cycle (u). This duty cycle value is

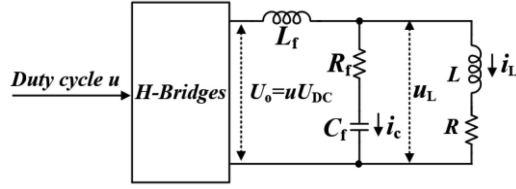


Fig. 4. Simplified model of a GPA power stage with $L_f = L_1 + L_2$; $R_f = R_3 + R_4$; $C_f = C_1 C_2 / (C_1 + C_2)$.

constant in PWM intervals and can only be changed at the end of the PWM intervals.

The dynamic systems must contain energy-storing elements, which can memorize the value of the input. The state variables related to these energy-storing elements can determine the internal state of the dynamic system. Therefore, I_c , I_L , U_L in Fig. 4 can be selected as the elements of the GPA state vector. Using the state equations of these three energy-storing elements, the GPA can be presented in a state space model as

$$\begin{aligned} \underbrace{\begin{pmatrix} sI_L \\ sU_L \\ sI_c \end{pmatrix}}_{\dot{\mathbf{x}}} &= \underbrace{\begin{pmatrix} -\frac{R}{L} & \frac{1}{L} & 0 \\ \frac{R_f}{L} & -\frac{(L+L_f)R_f}{L_f L} & \frac{1}{C_f} \\ \frac{R}{L} & -\frac{(L+L_f)}{L_f L} & 0 \end{pmatrix}}_{\mathbf{A}} \underbrace{\begin{pmatrix} I_L \\ U_L \\ I_c \end{pmatrix}}_{\mathbf{x}} \\ &+ \underbrace{\begin{pmatrix} 0 \\ \frac{R_f}{L_f} U_{DC} \\ \frac{1}{L_f} U_{DC} \end{pmatrix}}_{\mathbf{b}} u \\ y &= \underbrace{(1 \ 0 \ 0)}_{\mathbf{C}} \underbrace{(I_L \ U_L \ I_c)^T}_{\mathbf{x}} \end{aligned} \quad (1)$$

where \mathbf{A} is the system matrix, \mathbf{b} is the input vector, and \mathbf{C} is the output matrix. This continuous-time state space model can be converted to a discrete-time state space model by [30]

$$X(k+1) = e^{\mathbf{A}T} X(k) + e^{\mathbf{A}T} \int_0^T e^{-\mathbf{A}t} \mathbf{b} u(kT) dt. \quad (3)$$

Since the accuracy of the zero-order hold equivalent is limited, the exact PWM duty cycle of the applied voltage needs to be taken into account in high-precision control design. Thus, the integration part in (3) can be derived as

$$\begin{aligned} H_{\text{exact}} &= e^{\mathbf{A}T} \int_{\frac{T}{2}(1-u)}^{\frac{T}{2}(1+u)} e^{-\mathbf{A}t} \mathbf{b} dt \\ &= \mathbf{A}^{-1} \left(e^{\frac{T}{2}(1+u)\mathbf{A}} - e^{\frac{T}{2}(1-u)\mathbf{A}} \right) \mathbf{b}. \end{aligned} \quad (4)$$

By differentiating H_{exact} with respect to the duty cycle u , the small-signal linear model can be derived as

$$H_s = \frac{T}{2} \left(e^{\frac{T}{2}(1+u)\mathbf{A}} + e^{\frac{T}{2}(1-u)\mathbf{A}} \right) \mathbf{b}. \quad (5)$$

In the conventional inverter applications, the duty cycle is changed in the range of 0 to 1. However, in the MRI GPA, the current waveform is a trapezoidal shape with short rising and falling times, which are typically around 0.2 ms and less

than 1% of the period. Therefore, the GPA output current is a static dc current in most of the time. In addition, the GPA generates a precise zero current during the ‘‘blank time’’ of a pulse. Therefore, the duty cycle is always very small in GPA applications. Since the duty cycle is close to zero in the steady state, a first-order Taylor estimation can be used to simplify (5). The equation then becomes

$$H = T e^{\frac{T}{2}\mathbf{A}} \mathbf{b}. \quad (6)$$

As a consequence, the discrete-time state space model for the GPA can be derived as

$$X(k+1) = G X(k) + H u(k) \quad (7)$$

$$Y(k) = C X(k) \quad (8)$$

where $G = e^{\mathbf{A}T}$, $H = T e^{\frac{T}{2}\mathbf{A}} \mathbf{b}$, and $C = (1 \ 0 \ 0)$.

In order to improve the current pulse reproducibility and system precision, an integrator is required to eliminate steady-state errors. One of the methods to introduce an integrator into the state space model is to introduce a new state vector. The state vector is the integral of the difference between the output vector and the input reference. Using the state space output equation (8), the integral state equation can be rewritten as

$$v(k+1) = v(k) + C [G X(k) + H u(k)] - r(k+1) \quad (9)$$

where $v(k)$ is the integral vector and $r(k+1)$ is the GPA input.

Furthermore, the delays of the state vectors need to be modeled in the GPA state space model. By again utilizing the first-order Taylor approximation, the delays can be modeled as

$$y(n - \mathbf{N} - \tau) = (1 - \tau)y(n - \mathbf{N}) + \tau y(n - \mathbf{N} - 1) \quad (10)$$

where τ and N denote the fractional delays and integer delays, respectively.

Utilizing the above state equations, the GPA discrete-time state space model can be derived as, (11) shown at the bottom of the next page, where $N + \tau$ denotes a delay of $N + \tau$ sampling period; G_{1stRow} and H_{1stRow} represent the first row of the state space system matrix G and input matrix H , respectively; and v denotes the integration that stores the most recent value of the integration and is the sum of the deviation between input reference and output value.

B. Design Method of Multi-Rational-Delay Variables State Space Control System

The feedback parameters of the state space controller can be determined by a pole placement method [30]. The feedback control equation can then be derived as

$$u_k = -K X_k = -(K_{i_L}, K_{u_L}, K_{i_c}, K_{u1}, K_{u2}, K_{u3}, K_{int}) X_k \quad (12)$$

where u_k denotes the duty cycle and K denotes the vectors of the feedback control parameters.

The feedback control equation (12) represents a feedback control system using state variables with the same delay values. However, it is beneficial to use state variables with different rational delays in the state space control system because using the internal state variables with less delays can significantly

improve system dynamic performance. Moreover, it is not easy to obtain the state variables with the same delays accurately for many applications, either because of the different limitations in sampling speed between high-resolution analog-to-digital converter (ADC) and other ADCs or because the system requires a high-precise and noiseless feedback signal of the control objective that needs high-performance filters. In GPA applications, the output current I_L is the control objective, which needs to be highly precise. Therefore, high-performance filtering or a high-resolution ADC can be used to achieve the required accuracy, leading to more delays, whereas simple filters or ADCs with lower resolution but higher sampling rate can be used in other state feedback signals I_c and U_L , enabling fast feedback. These aspects lead to the integer or fractional delays in different feedback signals. The proposed multi-rational-delay variables state space controller aims to resolve these problems by enabling the state space controller to operate correctly with the feedback signals having different integer and fractional delays, which improves the GPA current pulse reproducibility through its better dynamic performance.

In MRI GPA application, it is advantageous for the variables related to the output filter U_L and I_c to have less delays since this can improve the dynamic performance by damping the output filter faster. Therefore, U_L and I_c can be assumed to only have one computational delay, and then the state vector becomes

$$\widehat{X}_k = \begin{pmatrix} I_L^{[N+\tau]} & U_L^{[1]} & I_C^{[1]} & u^{[N+1]} & u^{[N]} & u^{[N-1]} & \nu \end{pmatrix}^T. \quad (13)$$

The only difference between X_k and \widehat{X}_k is the measurement values of U_L and I_c with different delays. If a transformation can be applied to obtain X_k from \widehat{X}_k , then the new control equation can be established with the feedback state variables of less delays. In order to calculate the transformation matrices, the state space model (8) can be utilized since it has the predictive capability for the future states. Using the system state matrix g and input matrix h , a state variable $s^{[N]}$ with N delays can be

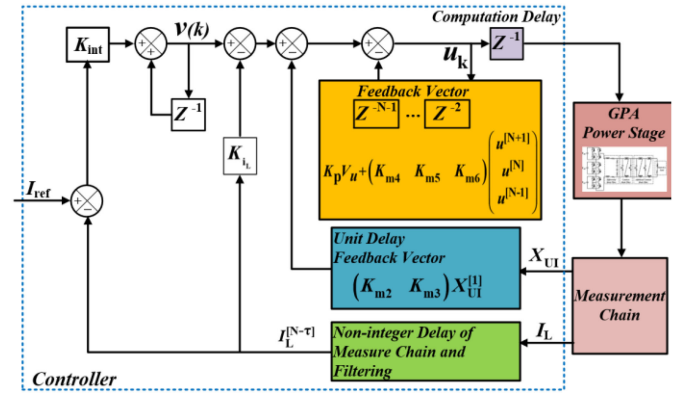


Fig. 5. Diagram of the proposed multi-rational-delay variables state space controller.

determined by its earlier state $s^{[N+1]}$ with $N+1$ delays as

$$s^{[N]} = g s^{[N+1]} + h u^{[N+1]}. \quad (14)$$

Also, the unit delay variables also need to be calculated from the rational delay variables in the GPA controller. Utilizing a first-order Taylor delay estimation, the state variables vector with rational delays can be presented by weighted state variables vector with integer delays, resulting in

$$s^{[N+\tau]} = (1-\tau) s^{[N]} + \tau s^{[N+1]}. \quad (15)$$

Therefore, the state vector $s^{[N]}$ can be obtained by substituting (15) into (14) and transposing, which yields

$$s^{[N]} = \underbrace{\left((1-\tau) E + \tau g^{-1} \right)^{-1}}_{\alpha} s^{[N-\tau]} + \underbrace{\tau h \left((1-\tau) g + \tau E \right)^{-1}}_{\beta} u^{[k+1]} \quad (16)$$

where E is an identity matrix. It is obvious that the state variables with smaller integer delays can be predicted by the past state

$$\underbrace{\begin{pmatrix} I_L^{[N+\tau]} \\ U_L^{[N+\tau]} \\ I_C^{[N+\tau]} \\ u^{[N+1]} \\ u^{[N]} \\ u^{[N-1]} \\ \nu \end{pmatrix}_{k+1}}_{X_{k+1}} = \underbrace{\begin{pmatrix} G & \tau H & (1-\tau) H & 0;0 \\ 0 & 0 & 0 & 0;0 \\ 0 & 0 & 0 & 0;0 \\ 0 & 0 & 0 & 0;0 \\ 0 & 0 & 0 & 0;0 \end{pmatrix}}_{G_{sys}} \underbrace{\begin{pmatrix} 1 & 0 & 0 \\ 0 & 1 & 0 \\ 0 & 0 & 1 \\ 0 & 0 & 0 \end{pmatrix}}_{(1-\tau) H_{1stRow}} \underbrace{\begin{pmatrix} I_L^{[N+\tau]} \\ U_L^{[N+\tau]} \\ I_C^{[N+\tau]} \\ u^{[N+1]} \\ u^{[N]} \\ u^{[N-1]} \\ \nu \end{pmatrix}_k}_{X_k} + \underbrace{\begin{pmatrix} 0 & 0 \\ 0 & 0 \\ 0 & 0 \\ 0 & 0 \\ 0 & 0 \\ 1 & 0 \\ 0 & -1 \end{pmatrix}}_B \begin{pmatrix} u_k \\ I_{ref,k+1} \end{pmatrix} \quad (11)$$

variables with larger rational delays, and this equation has the same structure as the state space model (7). Thus, the desired equation for a state variable with unit delay can be derived as

$$s^{[1]} = g^{N-1}\alpha s^{[N+\tau]} + g^{N-1}\beta u^{[N+1]} + g^{N-2}hu^{[N]} + g^{N-3}hu^{[N-1]} + \dots + hu^{[2]}. \quad (17)$$

Replacing the state variable s with the vector $X_{UI} = (U_L I_C)^T$, (17) can be applied in the GPA control system with these multi-rational-delay state variables, leading to the GPA multi-rational-delay state matrix as

$$\begin{pmatrix} I_L^{[N+\tau]} \\ U_L^{[1]} \\ I_C^{[1]} \end{pmatrix} = \begin{pmatrix} G_{1stRow} \\ G_1 G_{UI}^{N-1} \alpha \end{pmatrix} \begin{pmatrix} I_L^{[N+\tau]} \\ U_L^{[N+\tau]} \\ I_C^{[N+\tau]} \end{pmatrix} + \begin{pmatrix} \tau H_{1stRow} & (1-\tau) H_{1stRow} & 0 & \dots & 0 \\ & \eta & & & \end{pmatrix} V_u \quad (18)$$

$$\eta = (G_{UI}^{N-1} \beta \ G_{UI}^{N-2} H_{UI} \ \dots \ H_{UI}) \quad (19)$$

$$V_u = (u^{[N+1]} \ u^{[N]} \ \dots \ u^{[2]})^T \quad (20)$$

where G_1 denotes a column vector with the row 2 column 1 element and the row 3 column 1 element in G matrix, G_{UI} represents the square matrix with the elements of the row 2 to 3 and column 2 to 3 in G matrix, and H_{UI} indicates the second and third row of H matrix. Therefore, the values of U_L and I_C with unit delay can be written as

$$X_{UI}^{[1]} = G_{UI}^{N-1} \alpha X_{UI}^{[N+\tau]} + G_1 I_L^{[N+\tau]} + \eta V_u. \quad (21)$$

As a consequence, the transformation equation between X_k and \hat{X}_k can be written with the matrices M and P as

$$\underbrace{\begin{pmatrix} I_L^{[N+\tau]} \\ U_L^{[N+\tau]} \\ I_C^{[N+\tau]} \\ u^{[N+1]} \\ u^{[N]} \\ u^{[N-1]} \\ \nu \end{pmatrix}}_{X_k} = \underbrace{\begin{pmatrix} 1 & 0 & 0 & 0 & 0 & 0 \\ \hline -(G_{UI}^{N-1} \alpha)^{-1} G_1 & (G_{UI}^{N-1} \alpha)^{-1} & 0 & 0 & 0 & 0 \\ \hline 0 & 0 & 0 & 1 & 0 & 0 \\ 0 & 0 & 0 & 0 & 1 & 0 \\ 0 & 0 & 0 & 0 & 0 & 1 \\ 0 & 0 & 0 & 0 & 0 & 0 & 1 \end{pmatrix}}_M \underbrace{\begin{pmatrix} I_L^{[N+\tau]} \\ U_L^{[1]} \\ I_C^{[1]} \\ u^{[N+1]} \\ u^{[N]} \\ u^{[N-1]} \\ v \end{pmatrix}}_{\hat{X}_k} + \underbrace{\begin{pmatrix} 0 & -(G_{UI}^{N-1} \alpha)^{-1} \eta V_u & 0 & 0 & 0 & 0 \end{pmatrix}^T}_P. \quad (22)$$

Finally, the new state space feedback control equation using multi-rational-delay state vector can be established with a transformation by

$$\begin{aligned} u_k &= -K X_K = -K \left(M \hat{X}_k + P \right) = -K M \hat{X}_K - K P \\ &= - \underbrace{\left(K_{m1} \ K_{m2} \ \dots \ K_{m7} \right)}_{K_m} \hat{X}_K \\ &\quad - \underbrace{\left(K_{pN+1} \ K_{pN} \ \dots \ K_{p2} \right)}_{K_p} V_u. \end{aligned} \quad (23)$$

It is clear in (23) that the multi-rational-delay variables state space controller possesses the advantage of using state variables with less delays, enabling faster system response. Moreover, this design method can be used in both multiple sample-rate systems and single sample-rate systems, providing a flexible high-performance digital controller design approach. A diagram of the GPA multi-rational-delay variables state space controller is shown in Fig. 5.

III. RESOLUTION IMPROVEMENT METHOD FOR LOW CURRENTS

In MRI applications, the GPA is required to generate spurious-free zero current in the intervals of gradient pulses to avoid artifacts in the image. Moreover, the GPA should be able to generate precise low currents in order to cancel out the offsets in the MRI gradient subsystem. Therefore, the ability for high-resolution current generation at low current levels is an essential requirement for the MRI GPA. Using the multi-rational-delay variables state space control method derived in Section II, the precise control performance can be achieved at most output current levels. However, at zero or very low dc output current, precise current control cannot be realized mainly due to the nonlinear and uncontrollable region at low duty cycle, and the variation in parasitic parameters of the power switching devices in the H-bridges can lead to distorted pulses, producing spurious noise and enlarging the nonlinear region. To overcome this problem, an out-of-band signal injection method is proposed to achieve high-precision current at zero and low output range by reducing the nonlinear and uncontrollable region and the impact of the variations in parasitic parameters of the power switching semiconductor.

A. Spurious Noise at Low Output Currents

At zero or low output current levels, the duty cycle generated by the control system will be zero or close to zero. However, even though the duty cycle generated by the controller is zero or close to zero, the actual output current generated by the H-bridges is nonzero or not at the correct level due to the fact that the distorted small pulses at low duty cycle may not reach the dc-link voltage in which case the output voltage of the H-bridge is not proportional to the small duty cycle. In addition, these distorted small pulses also generate spurious signals in the output. The controller will then try to react to the incorrect output current, introducing a ripple in the desired output current

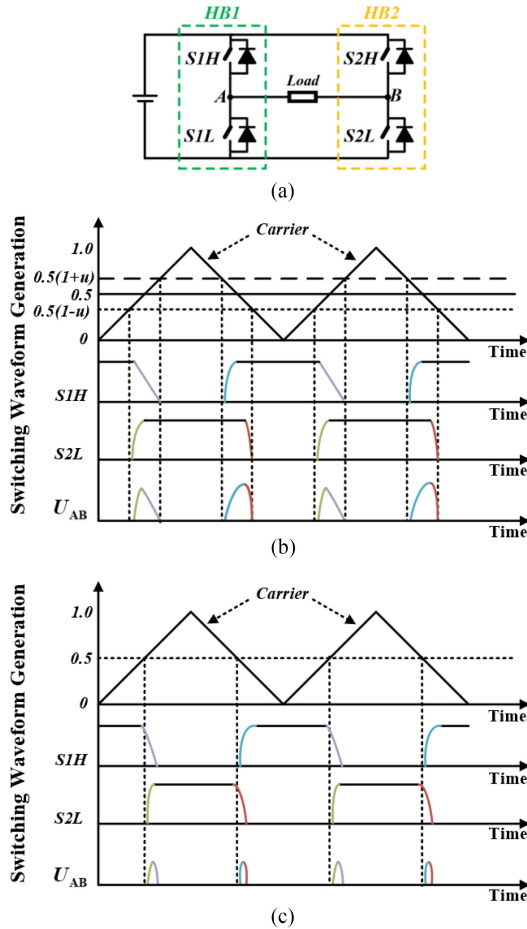


Fig. 6. Distorted output voltage generation by the exaggerated asymmetrical switching of power switching devices in an H-bridge. (a) Diagram of an H-bridge. (b) Switching waveform at very low duty cycle. (c) Switching waveform at zero duty cycle ($u = 0$). U_{AB} denotes the voltage between A and B.

that significantly reduces the resolution and signal-to-noise ratio at zero or very low current levels.

One of the key root causes to generate the distorted small pulses is the difference in parasitic parameters of each switching power device. Due to this variation of parasitic parameters, each switching power device has a slightly different switching characteristic, resulting in different turn-ON and turn-OFF transitions. This asymmetrical switching will introduce distorted pulses in the H-bridge output, leading to the generation of spurious noise. Each switching power device contributes noise energy by the rising and falling switching edges, and these energies add up together to create considerable noise in the final current output. Fig. 6 illustrates the mechanism of asymmetrical switching, caused by the variation in parasitic parameters. In this figure, the different colors and shapes in the exaggerated rising or falling edges denote the asymmetrical switching behavior at low duty cycle and indicate each group of energy that contributes to the spurious noise. Fig. 6(b) and (c) shows the exaggerated asymmetrical switching waveform under the conditions of very low duty cycle and zero duty cycle, respectively. It can be observed that distorted voltage waveforms are generated, leading to the generation of spurious noise current in the output.

This mechanism can be mathematically explained using Fourier transformation. Ideally, when all pulses are symmetrical, their Fourier transformation is equal to

$$FT_{\text{idea}} = 2 \sum_{k=-\infty}^{k=+\infty} \frac{\text{Sin}(k\omega_0 T_1)}{k} \delta(\omega - k\omega_0) \quad (24)$$

where T_1 is the pulswidth of each rectangular pulse and ω_0 is the angular frequency of the pulse series. Therefore, the noise spectrum only has components at harmonics of the switching frequency, and other frequency components do not show up in the output waveform. However, in practice, there will be a slight difference in the width of the individual pulses in the series, caused by the variance of the parasitic parameters in the switching power devices. The Fourier transformation of the actual pulse series, when taken as purely rectangular pulses, ignoring the rising and falling edges, can be obtained as

$$FT_{\text{actual}} = \sum_{n=0}^{n=+\infty} 2 T_n \text{Sinc}(\omega T_n) e^{-j\omega T_s n} \quad (25)$$

where T_n is the half pulse length in each pulse and T_s is the switching period. The main energy of (25) is within a frequency band of $[-\frac{\pi}{T_n}, \frac{\pi}{T_n}]$, indicating additional noise at unwanted frequencies. Therefore, the current resolution is reduced.

The other root cause is that the deadtime in the PWM reduces the accuracy of the feedback control, leading to a nonlinear and uncontrollable region at low duty cycle and an incorrect reaction of controller. The asymmetrical switching behavior caused by the variation in parasitic parameters broadens this nonlinear and uncontrollable region. Thus, the GPA precision at low output currents reduces significantly.

B. Out-of-Band Signal Injection Method to Improve GPA Low Current Resolution

One solution that could be considered to improve the output current resolution is to implement dead-time compensation. However, such dead-time compensation does not help in the case of zero or low dc output current for two key reasons. First, at zero or low dc output current, the duty cycle of the PWM waveform is too small to effectively activate the switching action of the switching devices, for example, insulated gate bipolar transistors (IGBTs), due to the impact of parasitic capacitors and inductors. Such a low duty-cycle and distorted PWM waveform can neither be well-controlled by the system feedback control algorithm nor by dead-time compensation. Fig. 6 shows the low duty control and output voltage waveform that is deviating from a rectangular waveform; this waveform cannot be controlled within the required accuracy. The second reason is that the significant ripple at the actual H-bridge output current may cross zero several times around the points when the load current is zero or low close to zero

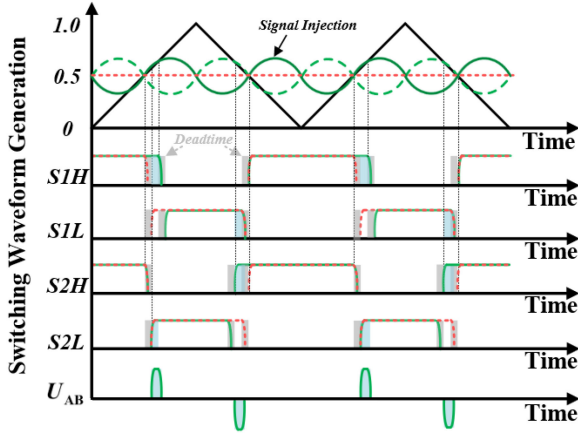


Fig. 7. PWM generation scheme at duty cycle $u = 0$ with out-of-band signal injection method (green) and without out-of-band signal injection method (red dashed).

[29]. These additional zero crossings will cause errors in current direction and polarity determination resulting in incorrect compensation.

A more appropriate way to achieve low spurious noise is to inject an out-of-band signal within the control loop. This out-of-band signal injection method improves the low current resolution in the following two ways. First, the out-of-band signal will create a nonzero duty cycle, leading to a nonzero current in the switching power devices, which charges the parasitic capacitors sufficiently. The switching actions of power devices now start with charged parasitic capacitors, which reduces the asymmetrical switching behavior and pushes the output current waveform toward the ideal rectangular waveform, weakening the generation mechanism of spurious currents. Second, the out-of-band signal injection method improves the accuracy of the feedback control by creating an offset in the duty cycle and thus shifting the operational point out of the nonlinear and uncontrollable region into the region where the feedback control algorithm works well. As a consequence, the system nonlinear and uncontrollable region is reduced and the resolution in the output current is improved. Fig. 7 shows the PWM generation scheme at zero duty cycle with the out-of-band signal injection method. It can be clearly seen that the offset voltage (U_{AB}) now is generated at zero duty cycle. Also, when the GPA system is operating with a small duty cycle to generate very low output current, this small duty cycle is now added to the shifted operation point. Thus, the GPA system works out of the nonlinear and uncontrollable region and therefore resolution is improved. Finally, since the injected signal is small in amplitude and out-of-band, it will be filtered out by GPA system. Therefore, no impact will be observed in the output current waveform. Fig. 8 illustrates the multi-rational-delay variables state space controller with the proposed signal injection method.

In order to select the correct frequency for the injected signal, the transfer function $G(z)$, which is the gain between the injected current and the GPA output current, can be derived by using the state space equations (11), (12), (22), and (23) as

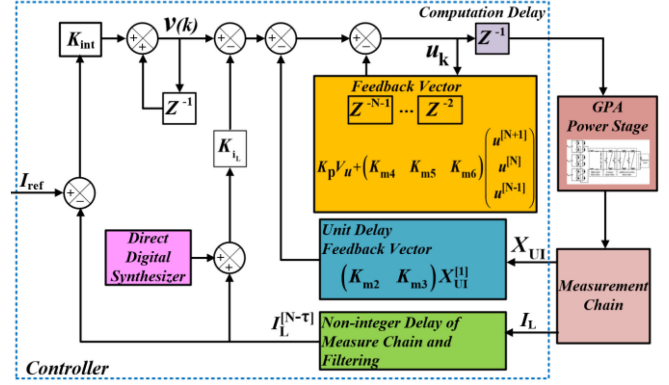


Fig. 8. Out-of-band signal injection control method in the multi-rational-delay variables state space controller.

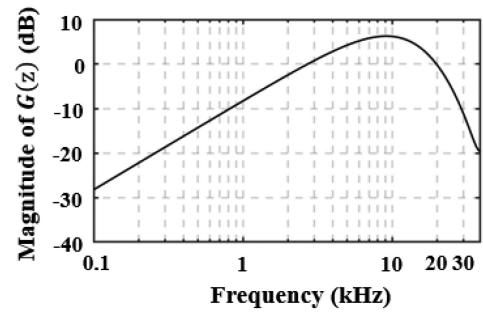


Fig. 9. Magnitude of $G(z)$ in the simulation of a GPA using three cascaded H-bridges with 15 kHz PWM switching frequency and 7 kHz system bandwidth.

follows [30]:

$$G(z) = - \frac{K_{iL} H_1(z)}{\left[1 + \left(K_{iL} + K_{int} \frac{z^{-1}}{1-z^{-1}} \right) H_1(z) + K_{m2} H_2(z) + K_{m3} H_3(z) + K_{m4} z^{-1} + K_{m5} z^{-2} + K_{m6} z^{-3} \right]} \quad (26)$$

$$H_1(z) = (1 \ 0 \ 0 \ 0 \ 0 \ 0) (zE - G_{sys})^{-1} B_1 \quad (27)$$

$$H_2(z) = (0 \ 1 \ 0 \ 0 \ 0 \ 0) (zE - G_{sys})^{-1} B_1 \quad (28)$$

$$H_3(z) = (0 \ 0 \ 1 \ 0 \ 0 \ 0) (zE - G_{sys})^{-1} B_1 \quad (29)$$

where E is an identity matrix and B_1 is the first column of the matrix B in the state space equation. Fig. 9 shows the magnitude of $G(z)$. It can be seen that this transfer function has a band-pass characteristic. The frequency of the injected signal needs to stay away from the frequency range of positive gain to avoid the amplification of the injected signal by the GPA. At the same time, the frequency of the injected signal cannot be selected too high to prevent low injection efficiency due to the attenuation by $G(z)$ and the switching frequency limitation of the high-power semiconductor. Therefore, a frequency range around twice of the switching frequency is a good choice. Considering the approximately -10 dB attenuation in $G(z)$ at twice the switching frequency, the signal magnitude needs to be less than 0.5 A to limit the magnitude of the injected signal

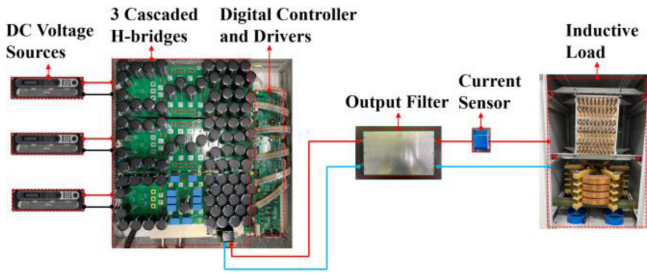


Fig. 10. Photographs of the main elements of the 1000 V/500 A GPA demonstrator.

TABLE I
TYPES AND PARAMETERS OF KEY EXPERIMENTAL INSTRUMENTS

Instrument	Model Type	Parameter
DC Voltage Source	SGI500X50D-1CAA	0-500 V, 0-50 A
Output Load	Inductive Load	L : 225 μ H, R : 65 m Ω
Current Sensor	ITN 900-S	900 A
Oscilloscope	MDO4104B-3	1 GHz
Current Probe	CWT6	1200 A, 16 MHz
IGBT	FF600R12IP4V	1200 V, 600 A
Digital Control Board	FPGA	Xilinx XC7Z100
High-resolution ADC	LTC2378	20 bits, 1 MSPS

in the GPA output to around 50 mA, which is the approximate noise floor of the GPA. Thus, the signal injection method can be turned ON in the full operational range of GPA since its leakage in the output current can be ignored. Experiments in Section IV will validate the effectiveness of this signal injection method and the method of the frequency and magnitude selection.

IV. EXPERIMENTAL VALIDATION

A 1000 V/500 A GPA demonstrator with the architecture illustrated in Fig. 3 is designed and built to validate the proposed analysis and control methods. Photographs of the main elements of the demonstrator are shown in Fig. 10. High-power IGBTs are used as switching power devices in the three cascaded H-bridges with around 7.5 mF capacitance for each H-bridge. The controller is realized in field-programmable gate array (FPGA) for high calculation speed and resolution. A conventional low-pass filter with around 12 kHz bandwidth is used in the output; the frequency of injected out-of-band signal is set to 30 kHz, which is twice the switching frequency, and the magnitude is set to 500 mA. The output current is measured with a high-resolution zero-flux-based current sensor ITN 900-S with 0.2 ppm noise below 100 Hz. The key experimental instruments are listed in Table I.

The proposed multi-rational-delay variables state space controller enables faster state vectors to be used in the controller, leading to around 60° phase margin and around 7 dB gain margin in the design for better system response with minimum

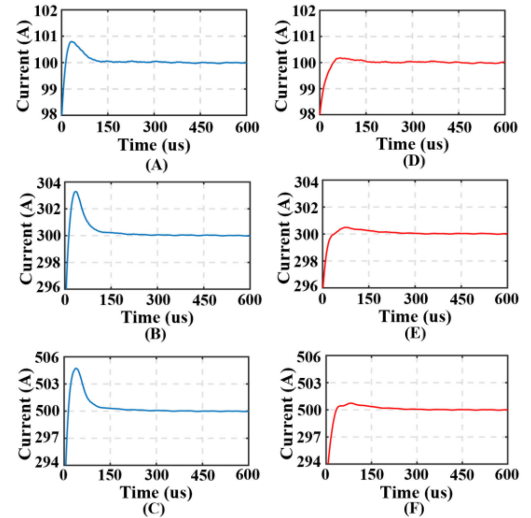


Fig. 11. Comparison of the step response in different current pulses with the state space controller using the same-delay state variables (A)–(C), and the multi-rational-delay variables state space controller (D)–(F) for currents of 100, 300, and 500 A, respectively (top, middle, bottom). (A) 100 A current pulse. (B) 300 A current pulse. (C) 500 A current pulse. (D) 100 A current pulse. (E) 300 A current pulse. (F) 500 A current pulse.

overshoot. A comparison of the step response in a state space controller using the same-delay state variables and the proposed multi-rational-delay variables state space controller is illustrated in Fig. 11. Both controllers are synchronized with the PWM switching frequency of 15 kHz and have the control cycle of around 11 μ s. In the proposed multi-rational-delay variables state space controller design, the state variables U_L and I_c , which represent the behavior of the output filter, are selected to have only a computational delay of one control cycle. The delay of the I_L data contains a mean filter of 16 consecutive data sampled at 1 MSPS by an ADC LTC2378, leading to a delay of around 2.5 control cycle together with a computational delay. This delay value in I_L is also used in the three variables of the conventional same-delay state space controller for comparison. Moreover, the control parameters are designed to achieve the same 7 kHz bandwidth in both methods for the performance comparison. It can be seen in Fig. 11 that the overshoot is reduced by approximately a factor of 8, leading to more similar pulse waveforms within one scan and therefore better current pulse reproducibility.

The other factor affecting the GPA performance is the variance of the latency in the current pulses during one MRI scan, which is in particular critical for short pulses. This critical factor has a strong relationship with GPA dynamic performance. Fig. 12 compares the latency variations in 64 trapezoidal current pulses as shown in Fig. 2 with the state space controller using the same-delay variables and the proposed multi-rational-delay variables state space controller. These trapezoidal pulses are triggered accurately by the FPGA with 100 ms intervals and each figure in Fig. 12 shows the middle region of the rising-edge of each trapezoidal current pulse by aligning the starting point to the same position for comparison. The latency variations become clearly much less using the proposed control method, with

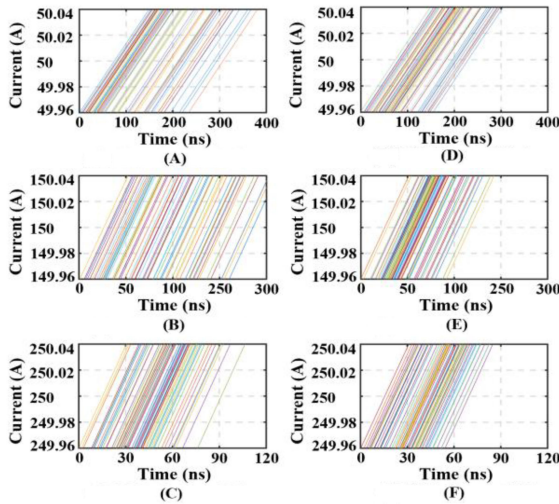


Fig. 12. Latency variations in 64 current pulses with the state space controller using the same-delay state variables (A)–(C) and the multi-rational-delay variables state space controller (D)–(F) for currents of 100, 300, and 500 A, respectively (top, middle, bottom). Each figure shows the middle region of the rising-edge of each current pulse by aligning the starting point to the same position for comparison. (A) 100 A current pulse. (B) 300 A current pulse. (C) 500 A current pulse. (D) 100 A current pulse. (E) 300 A current pulse. (F) 500 A current pulse.

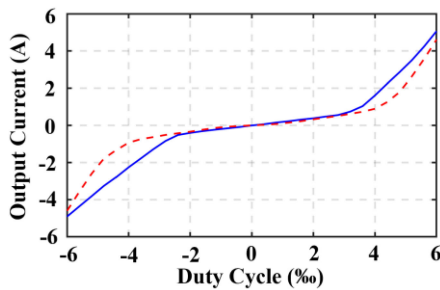


Fig. 13. Nonlinear and uncontrollable region at zero and low output currents without out-of-band signal injection (red, dashed) and with out-of-band signal injection (blue, solid).

reductions of 27%, 59%, and 39% for a 500, 300, and 100 A pulse sequence, respectively.

A key feature of the proposed control system, next to the multi-rational-delay variables state space controller, is the out-of-band signal injection method to reduce noise at zero and very low currents. Fig. 13 shows the nonlinear and uncontrollable region at zero and low output currents. As shown in Fig. 4, very low dc output current is generated by the GPA accurately in this experiment, driven by the duty cycle generated in the controller, illustrated as the horizontal axis of Fig. 13. It can be clearly seen in Fig. 13 that the nonlinear and uncontrollable region of the GPA system is reduced by more than 30% by the out-of-band signal injection method. Fig. 14 shows trapezoid waveforms with peak current amplitudes of ± 0.2 and 0 A with and without the signal injection method and the zoomed-in waveforms in the six positions. Fig. 15 shows a further performance comparison at zero and 0.2 A steady dc current. The data in the experiments are acquired by a high-resolution 20-bit ADC LTC2378 with a sampling rate of 1 MSPS, which samples the output of a

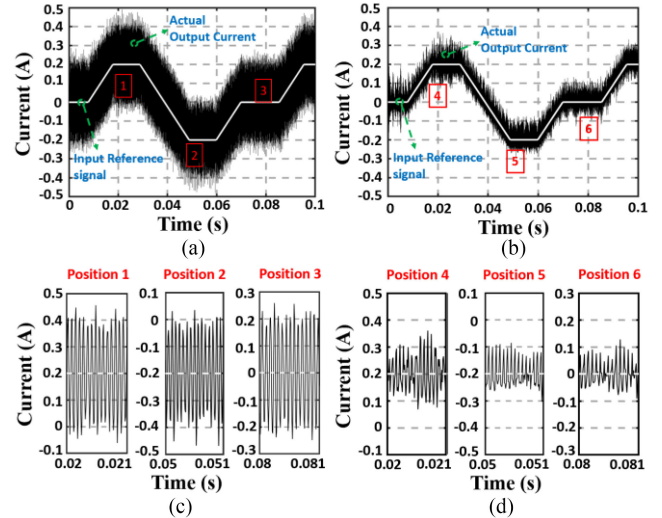


Fig. 14. Current in a trapezoidal waveform at zero and low output currents. (a) Without out-of-band signal injection. (b) With out-of-band signal injection. (c) and (d) contain the zoomed-in waveforms in the six positions in (a) and (b), respectively.

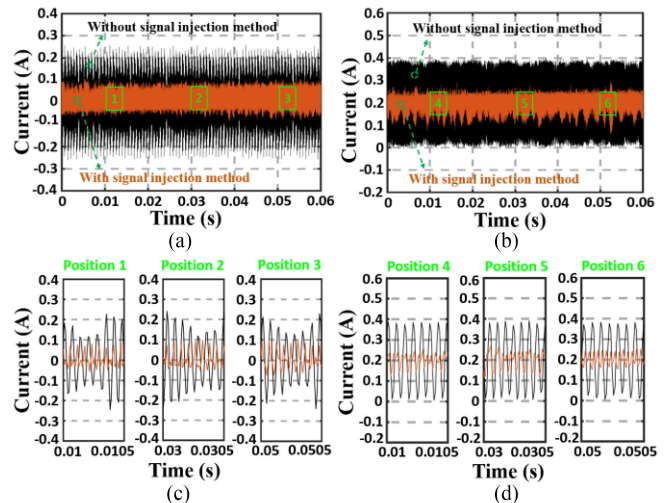


Fig. 15. Current at (a) 0 A and (b) 0.2 A dc output current, both without and with out-of-band signal injection. (c) and (d) contain the zoomed-in waveforms in the six positions in (a) and (b), respectively.

high-resolution zero-flux-based current sensor. The total number of the data is 10^5 and 6×10^4 in Figs. 14 and 15, respectively. The experimental results show a reduction by approximately a factor of 2.5 in the noise level at low currents by the out-of-band signal injection method. Fig. 16 illustrates the amplitude of GPA output noise as a function of injection signal frequency. The test is performed at 0 A input for the injected signals with different magnitude. Obviously, the noise level is the lowest with the 0.3 A signal injection. The 0.5 A signal injection provides too much energy in the injected signal, leading to an increase of the output noise level, whereas at 0.1 A signal injection, the energy is too low to effectively activate this method. It can be clearly observed that for 0.3 A signal injection, the frequency range around twice the 15 kHz switching frequency provides the

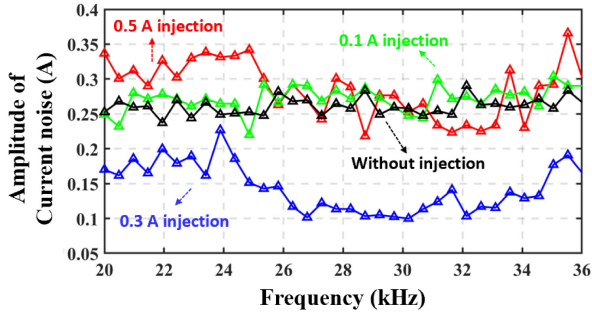


Fig. 16. Amplitude of GPA output current noise at 0 A input as a function of frequency of the injected signals, for different signal magnitudes. Green, blue, and black lines indicate test with 100, 300, and 500 mA injected signal, respectively. The black line is without signal injection.

TABLE II

COMPARISON OF NOISE GAIN WHEN USING THE OPTIMIZED PID CONTROLLER AND THE MULTI-RATIONAL-DELAY VARIABLES STATE SPACE CONTROLLER

Frequency Range (Hz)	100	500	1000	3000	5000	6000
Noise Gain-PID (dB)	-36	-23	-16	-13	-10	-5
Noise Gain-State Space (dB)	-60	-49	-37	-31	-26	-14

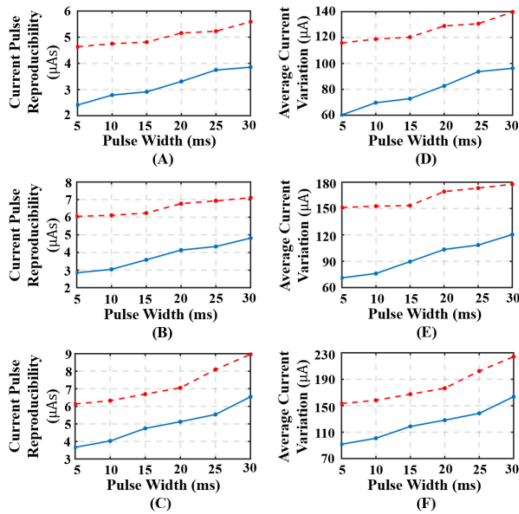


Fig. 17. Comparison of output current reproducibility (A)–(C) and average current variation (D)–(F) between the classical PID control method (red dashed) and the proposed multi-rational-delay variables state space controller (blue, solid) as a function of pulsewidth for currents of 100, 300, and 500 A, respectively. (A) 100 A current pulse. (B) 300 A current pulse. (C) 500 A current pulse. (D) 100 A current pulse. (E) 300 A current pulse. (F) 500 A current pulse.

lowest current noise. These results validate the effectiveness of the method for frequency and magnitude selection.

Table II presents the experimental test results of the PWM noise gain, which is the gain of the transfer function from the PWM generation to the GPA output, for both a classical PID control method and the control method developed in this article. Both controllers are tuned and optimized with the same power stage, and the bandwidths are both tuned to 7 kHz. Compared to

the PID controller, the proposed control method has at least ten times higher noise suppressing capability in a frequency band up to 6 kHz due to the availability of the internal state variables with less delay.

Finally, the output current pulse reproducibility of the GPA, one of the most critical performance parameters to achieve high MRI imaging quality, is compared in Fig. 17(a)–(c) with 40 ms integration time under different pulsewidths for the classical PID control method and the proposed control method. The current pulse reproducibility can also be transferred to average current variation by dividing integration time resulting in Fig. 17(d)–(f). It can be seen that the proposed control method has better current pulse reproducibility compared to the classical PID method for all current levels and pulsewidths, due to less noise power and higher control accuracy. In the experiment of 500 A maximum output current with 30 ms pulsewidth and 40 ms integration time as shown in Fig. 17(f), the PID controller has an average current variation of $224 \mu\text{A}$, whereas a $163 \mu\text{A}$ average current variation is achieved by the proposed control method. This corresponds to around 30% improvement in the current pulse reproducibility performance.

V. CONCLUSION

A high-precision control method based on a multi-rational-delay variables state space controller and an out-of-band signal injection approach is proposed and validated in this article that provides a solution for meeting the stringent requirements of high-power MRI GPA applications. A comprehensive design method of the state space controller with multi-rational-delay state variables together with a systematic modeling approach for the MRI GPA is introduced and analyzed in detail, enabling the multi-rational-delay state variables with less delay to be used in a state space control. A critical influencing factor affecting the GPA precision at low output current is analyzed, and an effective out-of-band signal injection solution is proposed. These proposed methods provide multiple benefits in high-precision GPA design in different aspects.

- 1) The multi-rational-delay variables state space control method enables improvement of the GPA dynamic performance by using internal state variables with less delays, leading to a reduction of overshoot and better current pulse reproducibility.
- 2) The out-of-band signal injection method is highly effective in suppressing noise at low current, which is a key advantage with respect to existing methods in the literature.
- 3) The multi-rational-delay variables state space controller design method can be used in both multiple sample-rate systems and single sample-rate systems, providing a flexible high-performance digital controller design approach. Also, the out-of-band signal injection approach can be independently implemented in different kinds of control methods for GPAs or high-precision converters.

A GPA demonstrator with 1000 V and 500 A output is designed and tested to validate the proposed control method. The experimental results show around eight times reduction in overshoot and approximately 40% improvement in the current

pulse latency variations with the proposed multi-rational-delay variables state space controller. There, furthermore, is a 2.5 times reduction in noise level at low currents using the out-of-band signal injection method and around 30% improvement in the current pulse reproducibility performance compared to a classical PID controller. These experimental results provide a convincing validation of the proposed comprehensive design method and prove its capability to contribute to significantly improved MRI image quality.

With the development of image-guided therapy, MRI systems with higher performance GPAs will be needed for improved image quality. The proposed design method for the precision improvement of high-power GPAs facilitates future high-performance GPA designs that meet these needs. In addition, the proposed design method could also benefit future high-resolution amplifier designs for other applications, such as nanoscale-positioning and subsea communication. Future research will focus on methods to complement the proposed control approach with a high-performance output filter and silicon carbide switching power devices.

ACKNOWLEDGMENT

The authors gratefully acknowledge all advice and technical support provided by the experts in Philips Healthcare Suzhou.

REFERENCES

- [1] D. W. McRobbie *et al.*, *MRI From Picture to Proton*, 2nd ed. Cambridge, U.K.: Cambridge Univ. Press, 2006.
- [2] E. Mark Haacke, R. W. Brown, M. R. Thompson, and R. Venkatesan, *Magnetic Resonance Imaging: Physical Principles and Sequence Design*. New York, NY, USA: Wiley-Liss, 1999.
- [3] O. M. Mueller, J. N. Park, P. B. Roemer, and S. P. Souza, "A high-efficiency 4-switch GTO speed-up inverter for the generation of fast-changing MRI gradient fields," in *Proc. 8th Annu. Appl. Power Electron. Conf. Expo.*, San Diego, CA, USA, 1993, pp. 806–812.
- [4] J. Sabate, L. Garces, P. Szczesny, Q. Li, and W. F. Wirth, "High-bandwidth high-power gradient driver for magnetic resonance imaging with digital control," in *Proc. 20th Annu. IEEE Appl. Power Electron. Conf. Expo.*, Austin, TX, USA, 2005, pp. 1087–1091.
- [5] L. Rixin, J. Sabate, S. Chi, and W. Skeffington, "High performance gradient driver for magnetic resonance imaging system," in *Proc. Energy Convers. Congr. Expo.*, Phoenix, AZ, USA, 2011, pp. 3511–3515.
- [6] J. A. Sabate, R. R. Wang, F. Tao, and S. Chi, "Magnetic resonance imaging power: High-performance MVA gradient drivers," *IEEE J. Emerg. Sel. Topics Power Electron.*, vol. 4, no. 1, pp. 280–292, Mar. 2016.
- [7] J. A. Sabate, L. Garces, P. Szczesny, Q. Li, and W. F. Wirth, "High-power high-fidelity switching amplifier driving gradient coils for MRI systems," in *Proc. IEEE 35th Annu. Power Electron. Spec. Conf.*, Aachen, Germany, 2004, pp. 261–266.
- [8] K. Corzine and Y. Familiant, "A new cascaded multilevel H-bridge drive," *IEEE Trans. Power Electron.*, vol. 17, no. 1, pp. 125–131, Jan. 2002.
- [9] R. Lai, L. Wang, and J. Sabate, "A high efficiency two-phase interleaved inverter for wide range output waveform generation," in *Proc. IEEE Energy Convers. Congr. Expo.*, Raleigh, NC, USA, 2012, pp. 4533–4537.
- [10] R. Lai, L. Wang, J. Sabate, A. Elasser, and L. Stevanovic, "High-voltage high-frequency inverter using 3.3 kV SiC MOSFETs," in *Proc. 15th Int. Power Electron. Motion Control Conf.*, Novi Sad, Serbia, 2012, pp. DS2b.6-1–DS2b.6-5.
- [11] R. Wang, J. Sabate, F. Tao, F. Xu, X. Liu, and C. Li, "H-bridge building block with SiC power MOSFETs for pulsed power applications," in *Proc. IEEE Energy Convers. Congr. Expo.*, Milwaukee, WI, USA, 2016, pp. 1–6.
- [12] M. Mauerer and J. W. Kolar, "Noise minimization for ultra-high SNR class-D power amplifiers," *CPSS Trans. Power Electron. Appl.*, vol. 3, no. 4, pp. 339–351, Dec. 2018.
- [13] M. Mauerer and J. W. Kolar, "Distortion minimization for ultra-low THD class-D power amplifiers," *CPSS Trans. Power Electron. Appl.*, vol. 3, no. 4, pp. 324–338, Dec. 2018.
- [14] M. Mauerer, A. Tüysüz, and J. W. Kolar, "Distortion analysis of low-THD/high-bandwidth GaN/SiC class-D amplifier power stages," in *Proc. Energy Convers. Congr. Expo.*, Montreal, QC, Canada, 2015, pp. 2563–2571.
- [15] R. Sepe and J. Lang, "Inverter nonlinearities and discrete-time vector current control," *IEEE Trans. Ind. Appl.*, vol. 30, no. 1, pp. 62–70, Jan./Feb. 1994.
- [16] J. W. Choi and S. K. Sul, "A new compensation strategy reducing voltage/current distortion in PWM VSI systems operating with low output voltages," *IEEE Trans. Ind. Appl.*, vol. 31, no. 5, pp. 1001–1008, Sep./Oct. 1995.
- [17] H. Fukuda and M. Nakaoka, "High-frequency ZVS PWM power amplifier for magnetic-field current tracking control scheme and its design considerations," in *Proc. Int. Conf. Power Electron. Drive Syst. Conf.*, Singapore, 1995, pp. 238–245.
- [18] J. A. Sabate, Q. Li, and W. F. Wirth, "Parallel operation of switching amplifiers driving magnetic resonance imaging gradient coils," in *Proc. Int. Power Electron. Motion Control*, Xi'an, China, 2004, pp. 1563–1567.
- [19] R. Wang, J. Sabate, Y. Mei, J. Xiao, and S. Chi, "Reduced common-mode noise modulation strategies for gradient driver with cascaded H-bridge multilevel structure," in *Proc. Energy Convers. Congr. Expo.*, Montreal, QC, Canada, 2015, pp. 240–246.
- [20] M. D. Bellar, T. S. Wu, A. Tchamdjou, J. Mahdavi, and M. Ehsani, "A review of soft-switched DC-AC converters," *IEEE Trans. Ind. Appl.*, vol. 34, no. 4, pp. 847–860, Jul./Aug. 1998.
- [21] S. Chen and W. T. Ng, "High-efficiency operation of high-frequency DC/DC conversion for next-generation microprocessors," in *Proc. Annu. Conf. IEEE Ind. Electron. Soc.*, Roanoke, VA, USA, 2003, pp. 30–35.
- [22] W. Ruxi, J. Sabate, Y. Mei, J. Xiao, and S. Chi, "Phase-shift soft-switching power amplifier with lower EMI noise," in *Proc. Energy Convers. Congr. Expo.*, Pittsburgh, PA, USA, 2014, pp. 2767–2772.
- [23] S. Karys, "Selection of resonant circuit elements for the ARCP inverter," in *Proc. 10th Int. Conf. Elect. Power Qual. Utilisation*, Lodz, Poland, 2009, pp. 1–6.
- [24] Y. Lee, J. Kim, B. Han, and J. Lee, "Auxiliary resonant commutated pole inverter with clamping diodes for voltage stress reduction across auxiliary switches," in *Proc. IEEE Region 10 Conf.*, Jeju, South Korea, 2018, pp. 394–398.
- [25] D. Leggate and R. J. Kerkman, "Pulse based dead time compensator for PWM voltage inverters," *IEEE Trans. Ind. Electron.*, vol. 44, no. 2, pp. 191–197, Apr. 1997.
- [26] J. S. Choi, J. Y. Yoo, S. W. Lim, and Y. S. Kim, "A novel dead time minimization algorithm of the PWM inverter," in *Proc. IEEE 34th IAS Annu. Meeting Ind. Appl. Conf.*, Phoenix, AZ, USA, 1999, pp. 2188–2193.
- [27] A. R. Muñoz and T. A. Lipo, "On-line dead-time compensation technique for open-loop PWM-VSI drives," *IEEE Trans. Power Electron.*, vol. 14, no. 4, pp. 683–689, Jul. 1999.
- [28] N. Hur, K. Nam, and S. Won, "A two-degrees-of-freedom current control scheme for deadtime compensation," *IEEE Trans. Ind. Electron.*, vol. 47, no. 3, pp. 557–564, Jun. 2000.
- [29] J. A. Sabate, L. Garces, P. Szczesny, and W. Skeffington, "Dead-time compensation for a high-fidelity voltage fed inverter," in *Proc. IEEE Power Electron. Spec. Conf.*, Rhodes, Greece, 2008, pp. 4419–4425.
- [30] K. Ogata, *Discrete-Time Control Systems*, 2nd ed. Englewood Cliffs, NJ, USA: Prentice-Hall, 1995.



Keqiu Zeng (Member, IEEE) was born in Fujian, China, in 1982. He received the B.S. and M.S. degrees from the University of Electronic Science and Technology of China, Chengdu, China, in 2005 and 2008, respectively.

From 2008 to 2010, he was with GE Global Research Center as a Research Scientist working on medical systems. Since 2011, he has been with the Philips Healthcare (Suzhou), Suzhou, China, and Philips Research, Shanghai, China, as a Senior Research Scientist, and since 2020, he has been an R&D Director. He leads various research activities related to power electronics and radio frequency electronics for medical systems. His research interests include packaging and integration in power electronics, wide bandgap power electronics, modern control, advanced digital signal processing, as well as radio frequency circuit and system.



Saijun Mao (Senior Member, IEEE) received the B.S. and M.S. degrees from the Nanjing University of Aeronautics and Astronautics, Nanjing, China, in 2003 and 2006, respectively, and the Ph.D. degree from the Delft University of Technology, Delft, The Netherlands, in 2018, all in electrical engineering.

From 2006 to 2017, he was a Senior Engineer and Project Leader with GE Global Research Center. He is currently a Research Fellow with Fudan University, Shanghai, China. His research interests include wide-bandgap power semiconductor devices based power conversion systems, high-frequency high voltage generator systems, as well as harsh environment power conversion and packaging.

Dr. Mao was the tutorial instructor in eight premier IEEE power electronics conferences. He has authored/coauthored more than 50 IEEE conference and journal papers. He holds more than 50 issued patents and pending patent applications. He was the recipient of one IEEE Best Paper Award, and more than 15 other awards, including Annual Technology Excellence Award, Annual Technology Excellence Team Award, and Top Inventor Award in GE Global Research Center.



Gert Rietveld (Senior Member, IEEE) received the M.Sc. (*cum laude*) and Ph.D. degrees in low temperature and solid-state physics from the Delft University of Technology, Delft, The Netherlands, in 1988 and 1993, respectively.

Since 1993, he has been with VSL, the National Measurement Institute of The Netherlands, Delft, The Netherlands, where he is currently the Chief Scientist with Electricity and Time Department. He has more than 25 years of experience in the area of electrical metrology, with his present work focusing on precision measurements for power and energy, and particularly metrology for smart electricity grids.

He is also a Full Professor with the University of Twente, Enschede, The Netherlands, where he holds the Chair of "Power and Energy Measurement Systems," working on precision measurements on batteries, measurement of power converter efficiency, and monitoring of electricity grids.

Dr. Rietveld chairs the European Metrology Network on Smart Electricity Grids. He is a member of the International Committee for Weights and Measures in Paris and the President of its Consultative Committee for Electricity and Magnetism. He is an active member of several IEEE, CIGRÉ, CENELEC, and IEC working groups.



Jelena Popovic (Member, IEEE) received the Dipl.Ing. degree from the Faculty of Electrical Engineering, University of Belgrade, Belgrade, Serbia, in 2001, and the Ph.D. degree from the Delft University of Technology, Delft, The Netherlands, in 2005.

From 2005 to 2011, she was with the European Center for Power Electronics as a Technology Transfer Coordinator. From 2008 to 2017, she was with the Delft University of Technology as an Assistant Professor. In 2018, she cofounded a start-up in energy

access, Klimop Energy. Since October 2019, she has been with the University of Twente, Enschede, The Netherlands, as a part-time Associate Professor to develop an energy access program. She has authored/coauthored more than 100 publications in scientific journals, magazines, and conferences. Her research interests include bottom-up solutions for energy access, appropriate technology, and socio-technical integration.

Dr. Popovic is the Vice-Chair of the IEEE PELS Technical Committee TC-12 Energy Access and Off-Grid Systems and the IEEE Empower a Billion Lives Competition.



Hui Yu (Member, IEEE) was born in Jiangsu, China, in 1988. He received the B.S. degree from the Nanjing University of Aeronautics and Astronautics, Nanjing, China, in 2008.

From 2011 to 2014, he was with Efore Suzhou as a Power Electronics Engineer. Since 2015, he has been with Philips Healthcare (Suzhou), Suzhou, China, as a Senior Power Electronics Engineer. His research interests include design and control of power electronics systems, high power density power system, and electrical magnetic interference.



Ligu Wang (Member, IEEE) was born in Zhejiang, China, in 1989. He received the B.S. degree from Lishui University, Lishui, China, in 2011, and the M.Sc. degree from Zhejiang University, Hangzhou, China, in 2013.

From 2013 to 2015, he was with the Shanghai Institute of Optics and Fine Mechanics. Since 2017, he has been with Philips Healthcare (Suzhou), Suzhou, China, as a Senior Digital Signal Processing Engineer. His research interests include advanced digital signal processing and modern control.



Kun Liu (Member, IEEE) was born in Chongqing, China, in 1976. He received the B.S. and M.S. degrees from Chongqing University, Chongqing, China, in 2003.

From 2004 to 2011, he was with the 10th Institute of China Electronics Technology and Huawei Hisilicon as a Digital Design Engineer. Since 2012, he has been with Philips Healthcare (Suzhou), Suzhou, China, as a Senior Digital Processing Engineer. His research interests include digital signal processing and soft define radio.



Zhiding Zhou (Member, IEEE) was born in Anhui, China, in 1992. He received the B.S. degree from the University of Central Lancashire, Preston, U.K., in 2014, and the M.S. degree from the University of York, York, U.K., in 2016.

From 2017 to 2020, he was with Nanjing Gova as a Design Engineer. Since 2020, he has been with Philips Healthcare (Suzhou), Suzhou, China, as a Digital Processing Engineer. His research interests include modern control and digital signal processing.